SP-284 — 11

Prediction of Concrete Integral Abutment Bridge Unrecoverable Displacements

WooSeok Kim, Jeffrey A. Laman, and Daniel G. Linzell

Synopsis: Integral abutment bridges (IABs) have performed successfully for decades and have demonstrated advantages over traditional, jointed bridges with respect to first cost, maintenance costs and service life. However, accurate prediction of IAB response to loading is complex and challenging; behavior is typically nonlinear due to the combined influence of thermal and long-term, time-dependent effects. Summarized herein are measured and computational results from examination of four interstate highway IABs located in central Pennsylvania. The collected data indicates that current AASHTO prediction methods are very conservative with respect to displacements. New computational models are used to perform a parametric study that considers the effects of seasonal thermal loading, thermal gradient, time-dependent material effects, abutment-backfill interaction and pile-soil interaction on deformations that occur over a 75-year bridge life. The measured and parametric study results provide a basis to establish an approximate method for predicting (1) maximum abutment displacement, (2) maximum bridge bending moments and (3) maximum pile moments over the bridge life.

Keywords: Integral Abutment, Bridges, Thermal Movement, Time-dependent, Nonlinearity

WooSeok Kim is an Assistant Professor in the Department of Civil Engineering, Chungnam National University, South Korea. His research interests include bridge engineering and structural reliability analysis.

Jeffrey A. Laman is a Professor in the Department of Civil and Environmental Engineering, Pennsylvania State University. His research interests include bridge response to vehicle loads and thermal loads, bridge design issues and bridge analysis methods, structural steel design innovations and analysis, and engineering education methodologies.

Daniel G. Linzell is the Shaw Professor of Civil Engineering at the Pennsylvania State University and the Director of the Protective Technology Center. His research interests include the behavior of bridges during construction and while in-service and force protection for buildings, bridges and other structures.

INTRODUCTION

It has been observed that integral abutment bridge (IAB) behavior is considerably different from that predicted by commonly employed analysis methods.[1] Thermal displacements measured at the abutment are 10 to 25 percent of predicted values. Thermally induced rotations and displacements are, in certain locations, in a direction opposite from predicted. In addition, thermally induced stresses are not commonly incorporated into widely available bridge member design aids and guidelines, however, stresses due to thermal loads are not insignificant. The most successful analysis and design will consider observed behavior such that the analysis accurately predicts the structural behavior.

The objective of this study was to develop IAB design criteria based on results of numerical parametric studies that are calibrated against in-situ measurements. Field monitoring was conducted at four integral abutment bridge sites using a wide range of instrumentation including strain gauges, pressure cells, extensometers, tilt meters and a weather station.[2,3] IAB engineering response data (displacement, rotation, strain, pressure) was continuously collected, compiled, processed, and evaluated from 2002 to 2008 at these four PennDOT bridges (109, 203, 211, and 222) on I-99 near Port Matilda, PA . Numerical parametric studies were then conducted on the basis of finite element models developed and calibrated against the observed integral abutment behavior. Results of the parametric studies were used to develop approximate analysis tools to simplify what is otherwise a very complex undertaking.

BRIDGE INSTRUMENTATION

The four IABs were selected to study a range of bridge lengths. Table 1 presents the major structural parameters of the selected IABs. All bridges in the study are right-bridges. A total of 240 instruments measuring girder and supporting pile strain and abutment displacement and rotation at four IABs were installed during bridge construction from Spring 2002 to Fall 2006. Data collection at bridges 203, 211, 222, and 109 began in November 2002, September 2004, November 2003, and July 2006, respectively.

IAB NUMERICAL MODEL

The IAB numerical model was developed using an available commercial numerical analysis package, ANSYS[5]. Bridge structural components were modeled as linear-elastic. Three important behaviors were identified as being important to capture and include: (1) soil-structure interaction; (2) nonlinear behavior of abutment-to-backwall joint; and (3) concrete time-dependent effects. Soil-structure interaction consists of two parts: (1) abutment-backfill interaction; and (2) soil-pile interaction. IAB loads include: (1) backfill pressure on abutments; (2) concrete superstructure time-dependent effects; (3) superstructure temperature change; and (4) temperature gradient along the superstructure depth. 2D numerical models were employed for the present study rather than 3D models to simulate the monitoring period due to the extreme computing demands of the iterative and non-linear analysis. Inclusion of prestressing steel relaxation, concrete creep and shrinkage, non-linear abutment-to-backwall construction joint rotation, and soil yielding within a time-history simulation requires extensive convergence iterations for each time step over a multi-year period. Simulations beyond two years were not possible with 3D models, therefore a careful effort was undertaken to develop reliable 2D models.

Table 1—Field Monitored IAB Geometry

Bridge No.	Girder Type	Integral Abutment	Abutment Height (H) ft (m)	Spans ft (m)	Length (L) ft (m)
109	PennDOT 28/78	Both	11.5 (3.5)	88-122-122-88 (26.8-37.2-37.2-26.8)	420 (128.0)
203	AASHTO V	North Only South Fixed	19.0 (5.8)	172 (14.3-26.8-11.30)	172 (52.4)
211	PennDOT 28/78	Both	14.1 (4.3)	114 (34.7)	114 (34.7)
222	PennDOT 24/48	Both	13.1 (4.0)	62 (18.9)	18.9 (62)

Notes:
1. Girder dimensions can be found in PennDOT DM-4.[4]
2. No restraints at intermediate piers.
3. Abutment height (H) is the height of backfill materials.

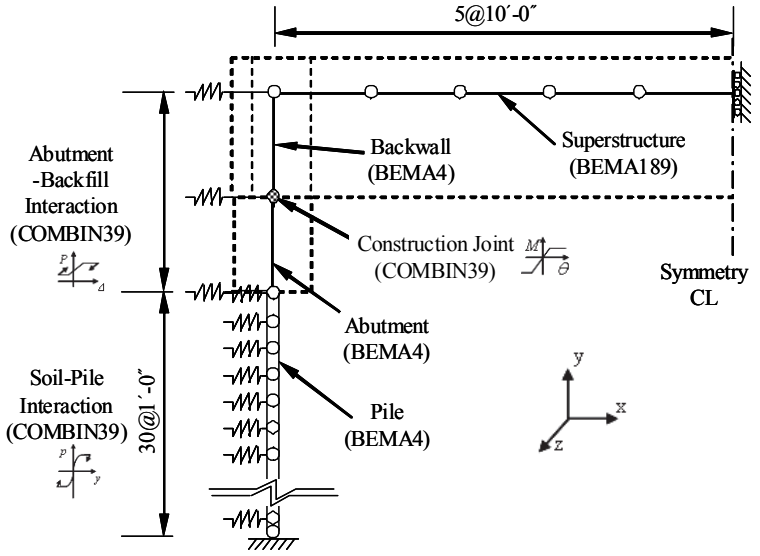

Fig. 1—Schematic of Numerical Model (1 ft = 0.31 m).

Table 2—Bridge Materials

Material	Strength (f_c' or F_y) ksi (MPa)		Elastic Modulus ksi (MPa)		Thermal Expansion Coefficient ºF (ºC)	
Precast Girder Concrete	8.0	(55.2)	5,150	(35,500)	6.0E-6	(10.8E-6)
Deck and Backwall Concrete	4.0	(27.6)	3,640	(25,100)	6.0E-6	(10.8E-6)
Parapet and Diaphragm Concrete	3.5	(24.2)	3,410	(23,500)	6.0E-6	(10.8E-6)
Pier and Abutment	3.0	(20.7)	3,160	(21,800)	6.0E-6	(10.8E-6)
Steel HP Piles	50	(345)	29,000	(200,000)	6.5E-6	(11.7E-6)

A schematic of the numerical model is presented in Fig. 1 with ANSYS element types identified. Material properties of each bridge component are presented in Table 2. Soil properties at all bridges were used in the parametric study; however, only one example soil type is presented in Fig.2. Detailed descriptions of the numerical model and material properties are documented elsewhere.[6-8]

The 2D numerical model assumes that the bridge is doubly symmetric, having a uniform deck slab thickness and evenly spaced, identical girders and supporting piles. At mid-length, the 2D model takes advantage of symmetry, expecting the bridge response to experience no *x*-axis translation or *z*-axis rotation (see Fig. 1). A single row of weak axis-oriented steel H-piles is modeled at the abutment. H-piles are embedded in the abutment and typically driven to bedrock, therefore, H-pile modeling does not incorporate soil friction or vertical displacement. The pile-abutment interaction is modeled at the abutment base with an equivalent translational (x-axis) nonlinear spring, a rotational (z-axis) nonlinear spring, and a vertical (y-axis) rigid support. The translational, x-axis and rotational z-axis spring properties are equated to fully model soil-pile interaction elements. The approach slab is not included in the longitudinal, nonlinear spring.

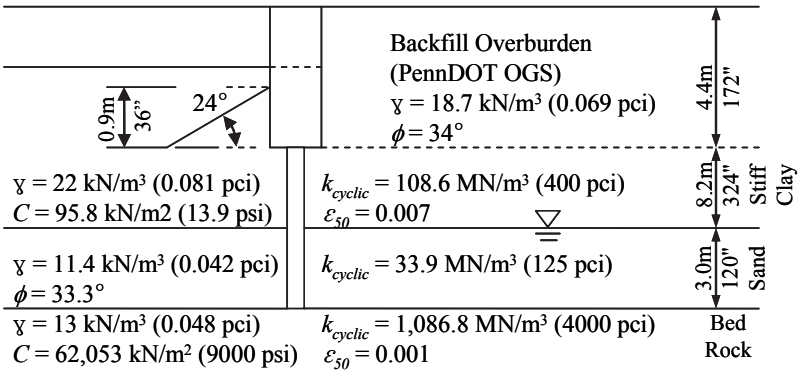

Fig. 2—Soil strata of Bridge 211 Abutment 1

Soil-Pile Interaction

Soil-pile interaction modeling requires an accurate representation of the piles and surrounding soil. For IABs, soil and pile resistance to longitudinal movement developed under bridge expansion is not the same as that for bridge contraction due to the different soil geometries in front of and behind the abutment. Soil resistance to bridge contraction is the result of a small soil overburden and downhill slope on the bridge side of the abutment. Soil resistance to bridge expansion is the result of a high and level soil overburden on the approach side of the abutment. This unequal soil resistance is the fundamental source of unequal structural response between bridge expansion and contraction.

The unrecoverable displacement characteristics of soil must also be considered when soil is subjected to cyclic loading. An elasto-plastic *p-y* curve proposed by Taciroglu *et al.*[9] was adopted in this research and is presented in Fig. 3. The elasto-plastic behavior is modeled through a finite element with an unloading branch using classical plasticity theory. A qualitative diagram of the elasto-plastic *p-y* curve is presented in Fig.3.

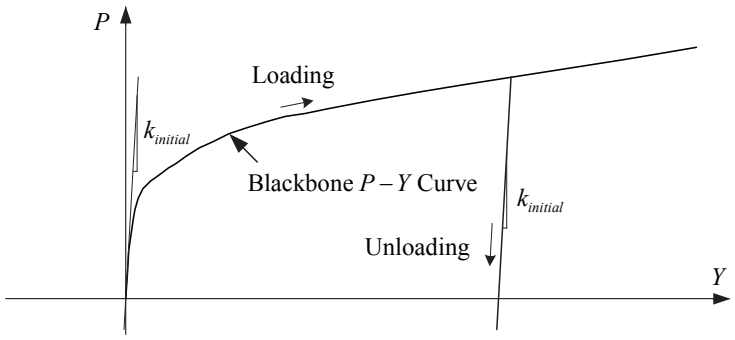

Fig. 3—Qualitative Diagram of Elasto-Plastic p-y Curve.

Abutment-Backfill Interaction

The abutment backfill interacts with the abutment and backwall. As the abutment and backwall move away from the backfill (bridge contraction), active earth pressure develops. When the abutment and backwall move toward the backfill (bridge expansion), soil resistance gradually increases up to the passive earth pressure limit after large displacements. Fig.4 presents a typical earth pressure versus displacement relationship with respect to abutment and backwall.

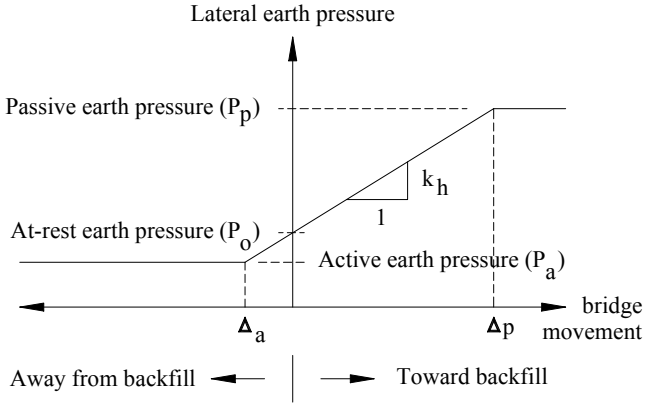

Fig. 4—Qualitative Lateral Earth Pressure at the Abutment and Backwall.

The prediction accuracy of abutment backfill pressure relies primarily on the determination of the coefficient of the lateral subgrade reaction, k_h. In the present study, k_h is determined from the slope of lateral displacements versus pressures obtained from extensometer and pressure cell data from the bridges that were studied. According to Boulanger *et al.*[10], the stiffness of granular soil is generally proportional to the square root of confinement. Thus, k_h at any depth, z, is expressed as:

$$k_h(z) = k_{ref}\left(\frac{z}{h_{ref}}\right)^{0.5} \quad (1)$$

where: h_{ref} = a reference depth measured from soil surface to the pressure cell elevation, z = a depth of the elevation of interest.

The relationships presented in Fig. 4 define the abutment-backfill interaction spring model for the finite element. In addition, the backfill exhibits a hysteretic response as defined by the force-displacement of cyclic loading and unloading. To incorporate this hysteretic behavior in the abutment backfill, classical plasticity theory is applied with the assumption that the unloading branch slope is parallel to the initial loading slope.

Abutment-Backwall Construction Joint

The joint required at the abutment-to-backwall connection is a common detail found in IAB construction. Steel reinforcement bar details of this joint vary from state to state[1-2]. The PennDOT standard IA joint detail specifies a "U" #5 bar at 9 inches (PennDOT Standard BD-667).[4] This joint reinforcement is much less than the reinforcement provided in the abutment and permits significant rotation between the superstructure and abutment. Although many previously completed studies assume that the abutment-to-backwall joint behaves rigidly, the cold joint condition and low reinforcing results in differential rotation as observed from field monitoring[1-2]. Paul *et al.*[11] demonstrated that the joint strength and stiffness determined from moment-curvature relationships are much lower than those calculated for abutments. Paul also proposed an elasto-plastic model for this abutment-to-backwall joint. To evaluate the joint and abutment stiffness, moment curvature relationships for the four monitored bridges were developed as presented in Fig. 5. Due to girder placement, the reinforcement area at the joint is different at the face toward the bridge and near the face toward backfill. Fig. 6 illustrates construction joint behavior with respect to superstructure expansion and contraction.

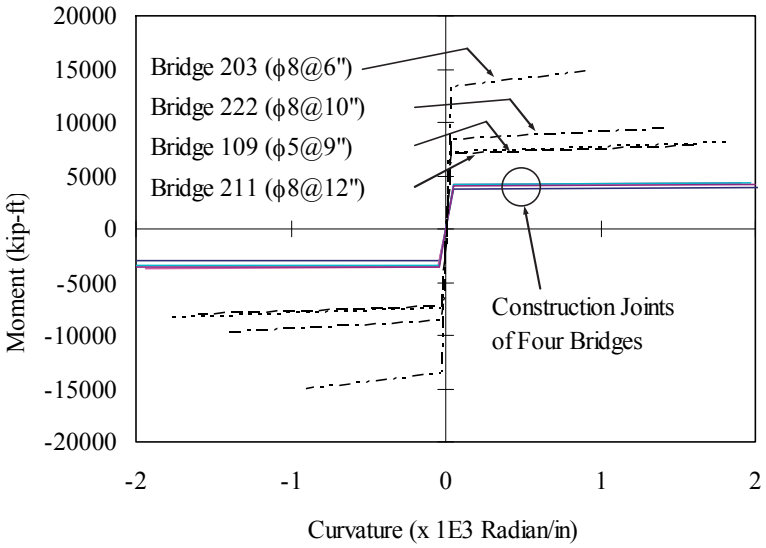

Fig.5—Moment-Curvatures for Construction Joints and Abutment Members (1 kip = 4.45 kN, 1 ft = 0.305 m).

The rotational strength and stiffness of the expansion case are greater than the contraction by about 20 percent. To convert joint moment-curvature to moment-rotation for element stiffness properties in the numerical model, NCHRP Recommended Provisions, 2000; and Paul[11] were used:

$$\theta = \int_0^L \frac{M}{EI} dx = \frac{M}{EI} L = \phi L \qquad (2)$$

Thermal Expansion Coefficient

All girders and the deck are modeled as a single beam element located at the centroid of the composite section with composite beam section properties. All materials are modeled as responding in the linear-elastic range for the thermal loading analysis. The superstructure is divided into beam elements incorporating equivalent gradient temperature loads, time-dependent loads, and prestress losses. In the case of steel girders with a concrete deck, the composite superstructure is constructed of materials with a dissimilar thermal expansion coefficient, therefore, the following equivalent thermal expansion coefficient, α_{eq}, is determined:

$$\alpha_{eq} = \frac{\alpha_g E_g A_g + \alpha_d E_d A_d}{E_g A_g + E_d A_d} \qquad (3)$$

where: α_g = girder material thermal expansion coefficient, E_g = girder elastic modulus, A_g = sum of girder sectional area, α_d = deck material thermal expansion coefficient, E_d = deck elastic modulus, A_d = sum of deck sectional area.

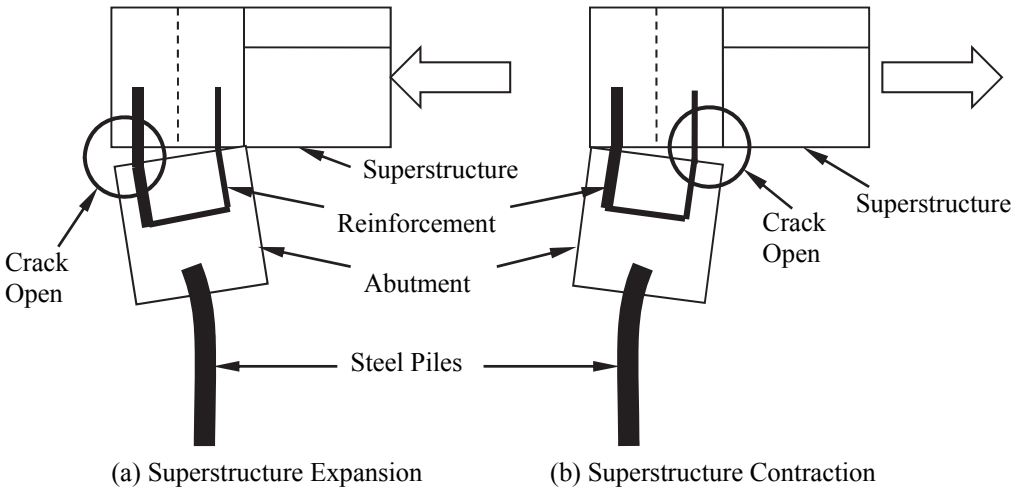

Fig. 6—Construction Joint Reinforcement and Behavior.

Temperature Fluctuation over 75-year Bridge Life

Superstructure temperature fluctuation over time is simulated with a sinusoidal curve that is based on field-collected data at monitored bridges and the locally positioned weather station. The 2D model is configured to simulate a 75-year bridge life; therefore, the sinusoidal temperature simulation must represent a nominal temperature fluctuation over the expected bridge life. Although bridge structures possess relatively low thermal conductivity and high thermal inertia, the average superstructure temperature is reasonably assumed to equal the ambient temperature. The temperature fluctuation is plotted in Fig. 7.

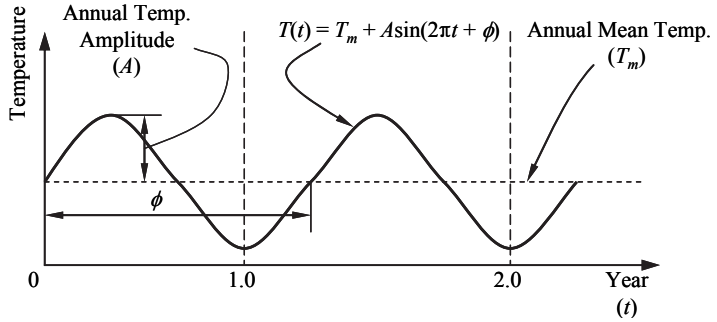

Fig. 7—Temperature Model.

Depending on the availability of local meteorological data, the annual mean temperature, temperature amplitude, frequency ($2\pi t$) and phase lag (ϕ) can be determined. Based on the present study monitoring results and information obtained from the National Climate Data Center, central Pennsylvania annual mean temperature equals 49 ºF and the annual temperature amplitude is 30 ºF. A phase lag of π is adopted when the bridge backwall concrete is placed during the fall season around the annual mean temperature.

Thermal gradient

Based on AASHTO[12] multi-linear temperature gradient requirements, an equivalent temperature gradient is computed. Thermal stress, σ_t, induced by the temperature gradient along the superstructure depth is represented as:

$$\sigma_t(y) = E \cdot \alpha \cdot T(y) \quad (4)$$

where: y = distance from the extreme bottom fiber, $\sigma_t(y)$ = longitudinal thermal stress at a fiber located at y; E = elastic modulus; α = thermal expansion coefficient, and $T(y)$ = temperature at y. Thus, the axial force, P_t, and moment, M_t, due to thermal stresses are:

$$P_t = \int E\alpha T(y)b(y)dY \text{, and}$$
$$M_t = \int E\alpha T(y)b(y)YdY \tag{5}$$

The AASHTO temperature gradient defines maximum and minimum gradients across the superstructure where summer results in the maximum temperature gradient and the minimum occurs during winter.

Time-dependent material effects

Time-dependent effects of creep, shrinkage, and prestressing steel relaxation significantly influence long-term behavior. The procedure described and summarized herein is based on CEB-FIP[13] and ACI209 (2004)[14]. Total strain in a concrete member can be expressed as:

$$\varepsilon(t) = \varepsilon_\sigma + \varepsilon_{cr} + \varepsilon_{sh} = \frac{\sigma(t_o)}{E(t_o)}\left[1 + \varphi(t,t_o)\right] + \varepsilon_{sh} \tag{6}$$

where: $\varepsilon(t)$ = total concrete strain at analysis time t due to constant stress at analysis time t due to constant stress, ε_σ = the immediate strain due to applied stress, σ, ε_{cr} = the time-dependent creep strain, ε_{sh} = free shrinkage strain, $\sigma(t_o)$ = the initial stress at the initial loading time t_o, $E(t_o)$ = modulus of elasticity at t_o, $\varphi(t,t_o)$ = creep coefficient at time t corresponding to the age at loading t_o. However, Equation 6 cannot be used directly because the applied stress, σ, is dependent on time. Fig. 8 illustrates the strain relationship to stress. To consider the strain variation, the effects of a series of applied stresses are determined individually, and then, all strains are combined based on the principle of superposition. For stress variation, Jirásek and Bažant[15] used the aging coefficient, χ, to adjust the creep coefficient.

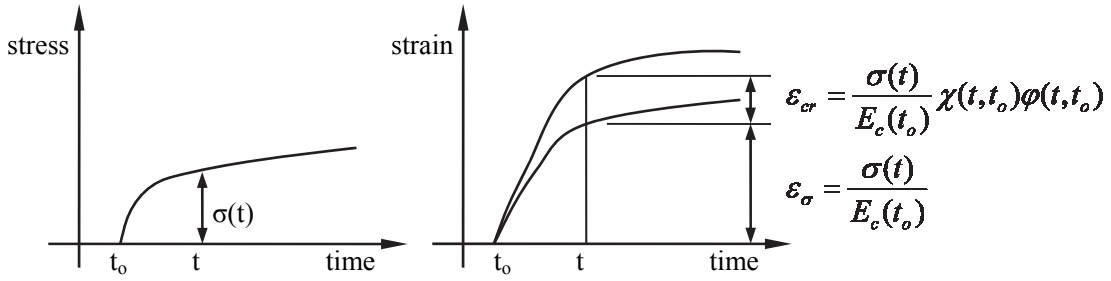

Fig. 8—Concrete Strain under Variable Stress.

When the applied stress is variable, the strain is calculated as:

$$\varepsilon = \frac{\sigma(t)}{E_c(t_o)}\left[1 + \chi(t,t_o)\varphi(t,t_o)\right] + \varepsilon_{sh} \tag{7}$$

For time-dependent elastic modulus variation, the effective modulus (E_c^*) method simplifies creep analysis because the method allows a pseudo-elastic analysis within a given time interval. E_c^* relates the immediate strain and time-dependant strain and is defined as:

$$E_c^*(t,t_o) = \frac{E_c(t_o)}{1 + \chi(t,t_o)\varphi(t,t_o)} \tag{8}$$

The aging coefficient can be precisely computed and tabulated by ACI 209[14], but $\chi = 0.7$ for a relatively young concrete age and $\chi = 0.8$ for all other uncertainties generally produces sufficiently accurate results. The ACI 209 shrinkage prediction equation is:

$$\varepsilon_{sh}(t) = \frac{t - t_o}{55 + (t - t_o)} \alpha \gamma_{sh} \tag{9}$$

where: α = a constant equal to 0.00078, γ_{sh} = a value determined by ambient relative humidity and size, shape effect, concrete slump test, fine aggregate percentage, and air content in concrete. Most prestressing strand steel exhibits relaxation that is similar to creep in that relaxation and creep both result in a loss of prestressing and concrete compressive stress. AASHTO[12] specifies determination of intrinsic relaxation of prestressing steel for low-relaxation strand as:

$$\Delta f_{RE} = \frac{[\log(24t) - \log(24t_o)]}{40} \left[\frac{f_{pj}}{f_{py}} - 0.55 \right] f_{pj} \tag{10}$$

Where: f_{pj} = prestressing jacking stress (ksi), f_{py} = yield strength of prestressing steel (ksi). However, Equation 10 describes the intrinsic relaxation, while the relaxation of prestressing steel is relieved due to the effects of elastic shortening, creep, and shrinkage. An approximate reduced relaxation coefficient χ_r was derived by Ghali[16]. The reduced relaxation, Δf_R, is expressed as:

$$\Delta f_R = \chi_r \Delta f_{RE}$$

$$\chi_r = \exp[(-6.7 + 5.3\lambda)\Omega]$$

$$\lambda = \frac{\text{steel stress immediately after transfer}}{\text{characteristic tensile stress}} \tag{11}$$

$$\Omega = \frac{\text{total prestress change - intrinsic relaxation}}{\text{steel stress immediately after transfer}}$$

However, for low-relaxation prestressing steel, the relaxation effects are very small compared to creep and shrinkage. Thus, in most practical situations, a factor of 0.8 may be applied to the relaxation portion for reducing strain. Therefore, the total strain due to time-dependent effects is expressed as:

$$\varepsilon(t) = \frac{\sigma(t_o)}{E_c(t_o)}[1 + \varphi(t, t_o)] + \frac{(\sigma(t) - \sigma(t_o))}{E_c^*(t, t_o)} + \varepsilon_{sh}(t, t_{sh,o}) \tag{12}$$

Backfill Pressure

Backfill pressure is represented as a triangular distribution along abutment depth based on a unit weight of porous granular backfill. Initially applied backfill pressure is based on the at-rest lateral earth pressure coefficient of K_o = 1.0 (compacted condition). The lateral earth pressure coefficients are varied between passive and active pressure. An equivalent hydrostatic pressure corresponding to the backfill depth is applied to the backwall and abutment to represent at-rest soil backfill pressure. Execution of the numerical analysis is completed in two stages: (1) an initial analysis to compute the displacements at each abutment-backfill interaction springs due to the at-rest pressure; and (2) the previously computed at-rest displacements are applied as initial displacements at the other end of the interaction elements and then at-rest soil pressure is externally applied. This procedure results in the abutment-backfill interaction spring to be in the zero-force state, but the abutment is subjected to the at-rest pressure. The abutment-backfill interaction spring must be modified as presented in Fig. 4.

VALIDATION OF NUMERICAL MODEL

Due to the inherent structural continuity between piles, abutments, backfill, and girders, an accurate numerical modeling of IAB systems is complex. An accurate IAB modeling process requires the inclusion of material property identification and representation (concrete, steel, soil, elastomeric, foam, etc.), environmental and time-dependent load modeling, and boundary condition modeling of critical bridge components. For the present study, measured material properties and dimensions as presented in Table 2 have been used in all presented analyses[1, 2]. The numerical model responses have been compared to measured responses where available. Abbreviated comparisons between predicted and measured responses are presented in Figures 10 and 11. The predicted and measured results follow the same trend and are reasonably well matched given the complexity.

PARAMETIC STUDY AND PREDICTION MODELS

Approximate analysis models are a desirable tool for complex design problems where preliminary results are needed prior to proceeding using a more sophisticated analysis. The results of this parametric study were evaluated using a standard regression analysis and form the basis of an approximate analysis prediction model for IABs. This approximate analysis method is applicable to short to medium-length bridges (100 ft to 400 ft) and determines five key responses: (1) abutment/pile-head displacement, (2) superstructure bending moment, and (3) pile-head moment. The approximate analysis requires five input parameters: (1) a concrete thermal expansion coefficient; (2) bridge length; (3) backfill height; (4) backfill stiffness; and (5) pile soil stiffness. The definition and determination of backfill height is illustrated in Fig. 9. Backfill soil properties and soil layers around piles are classified into three levels as presented in Tables 3 and 4. Soil stiffness properties have been classified as low, intermediate, and high stiffness.

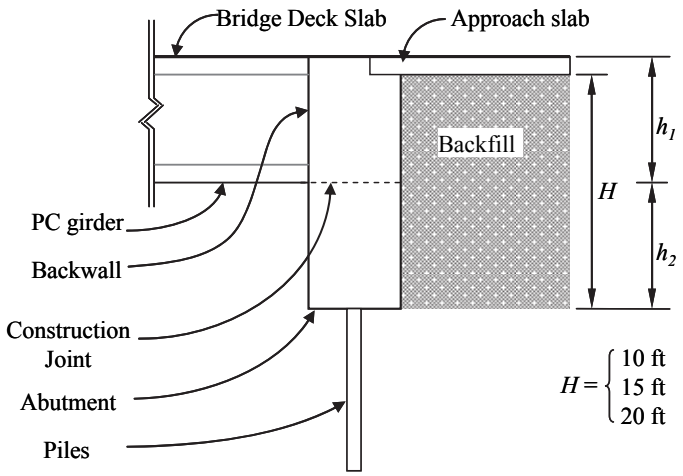

Fig. 9—Backfill Height Parameter (1 ft = 0.305 m).

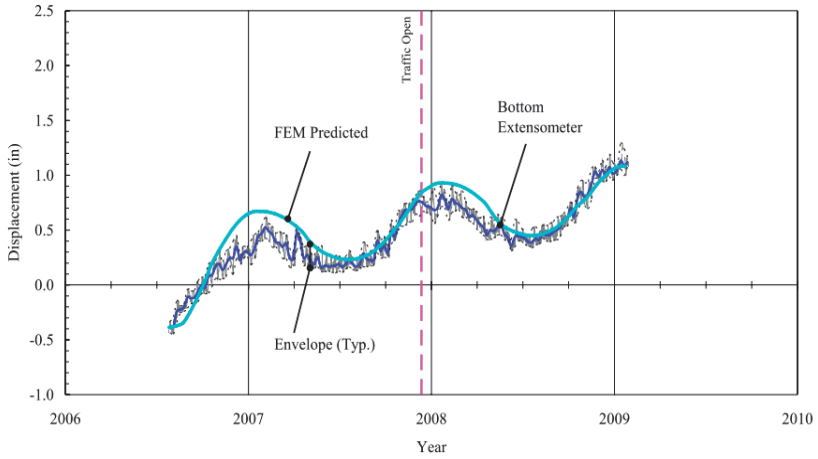

(a) Bridge 109

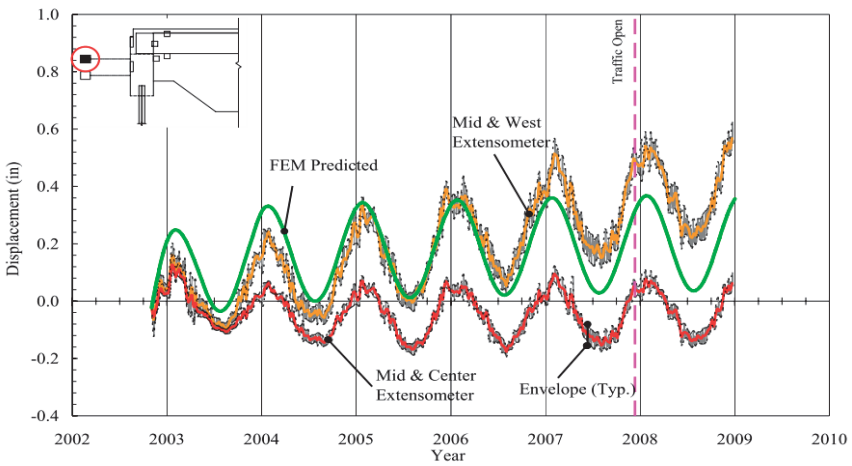

(b) Bridge 203

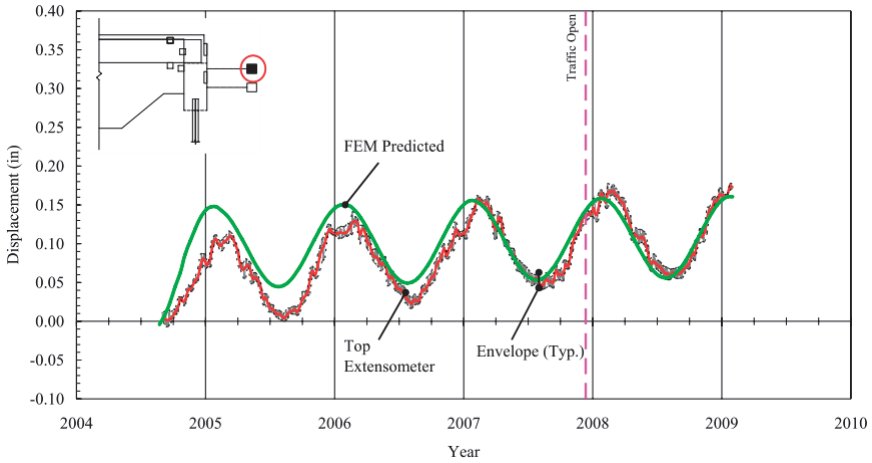

(c) Bridge 211

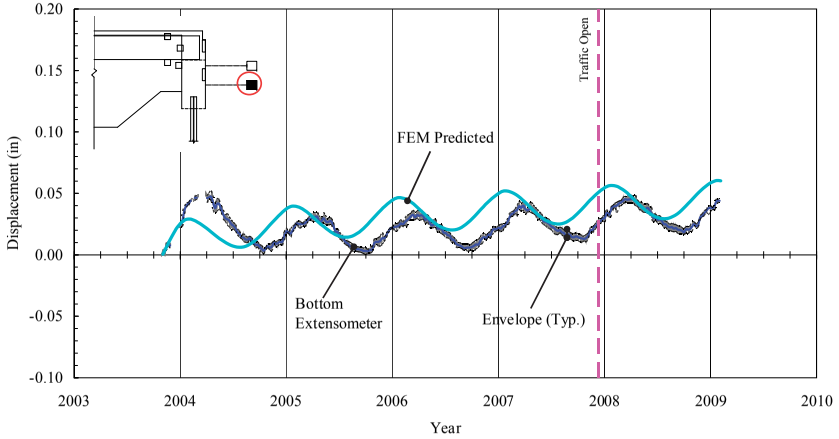

(d) Bridge 222

Fig. 10—Measured and predicted IAB abutment displacement (1 in = 25.4 mm).

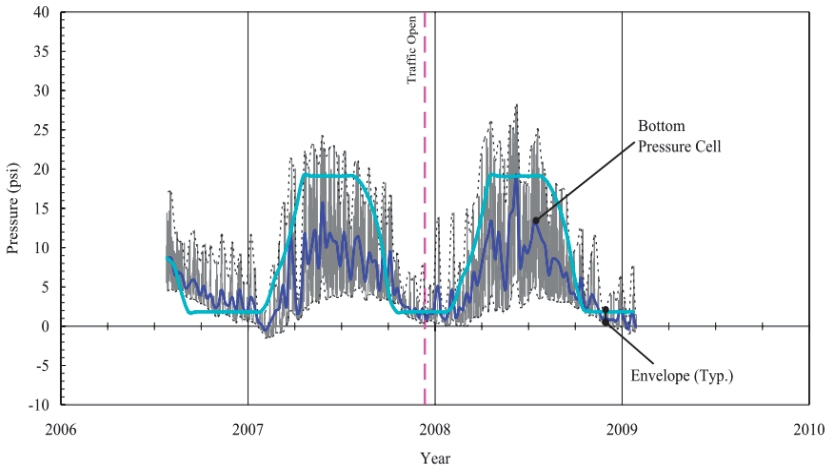

(a) Bridge 109

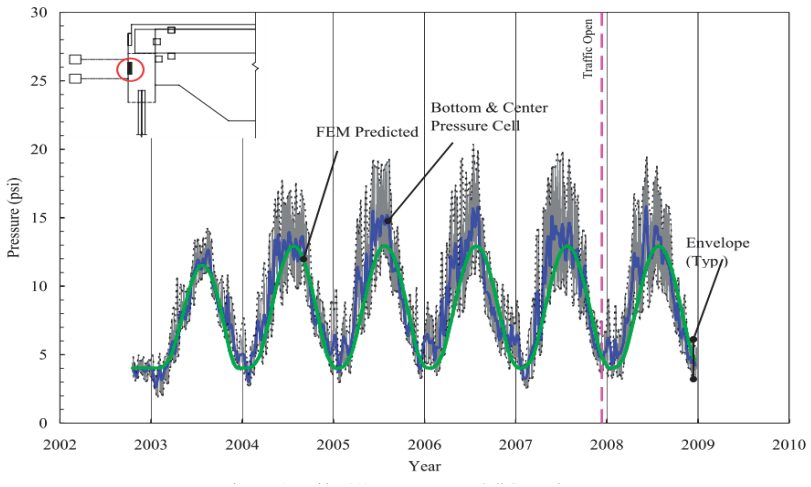

(b) Bridge 203

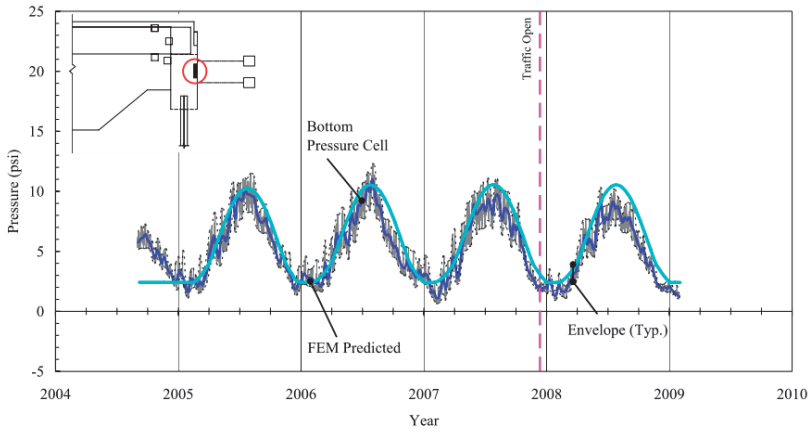

(c) Bridge 211

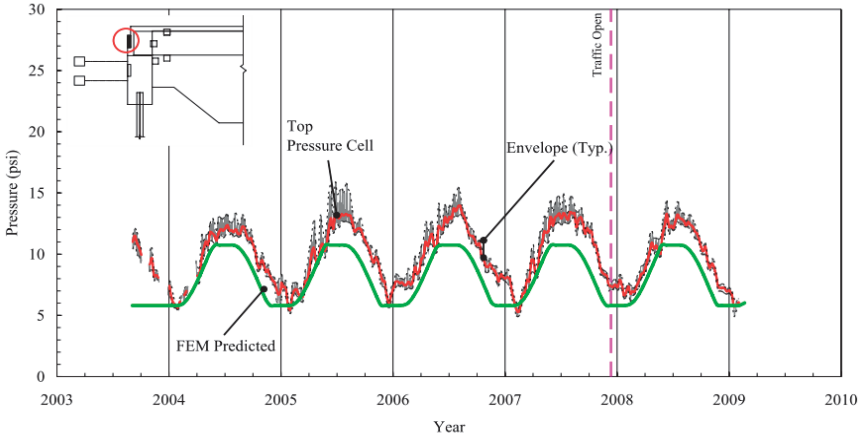

(d) Bridge 222

Fig. 11—Measured and predicted abutment backfill pressure (1 psi = 6.895 kPa).

Table 3—Backfill Properties and Range Determination (1 in = 25.4 mm, 1 lb = 4.448 N).

Property	*Low*	*Intermediate*	*High*
Density (γ) (pcf)	116	119	123
Angle of friction (ϕ_f) (Degree)	30.6	34	37.4
Subgrade Modulus (K_h) (pci)	22.5	43.8	65

Note: *Low* = 1, *Intermediate* = 2, *High* = 3 in the approximate method.

Table 4—Soil Layer Properties and Range Determination (1 in = 25.4 mm, 1 lb = 4.448 N).

Property	*Low*	*Intermediate*	*High*
Sand Density (pcf)	100	121	142
Clay Density (pcf)	100	121	142
Angle of Friction (Sand) (Degree)	28	35	42
Undrained Shear Strength (clay) (psi)	7	17.5	28
Elastic Modulus (K) (pci)	700	1000	1,300
ε_{50}, (in)	0.01	0.008	0.005

Note: *Low* = 1, *Intermediate* = 2, *High* = 3 in the approximate method.

Abutment/Pile-head Displacements

Due to bridge superstructure contraction and expansion, the pile head experiences lateral displacement, with the maximum displacement occurring at the pile head. The maximum pile-head displacement can be estimated as:

For prestressed concrete girder IABs:

$$u_{max} \quad \begin{cases} = 0.0004\alpha^{0.3}L^{1.2}B^{0.02}P^{-0.06} & \text{for } H \le 13\text{ft} \\ = 0.0006\alpha^{0.7}L^{1.0}B^{-0.02}P^{-0.1} & \text{for } 13 \le H \le 18\text{ft} \\ = 0.2\alpha^{0.3}L^{0.1}B^{-0.02}P^{-1.0} & \text{for } H \ge 18\text{ft} \end{cases} \qquad (13)$$

For steel girder IABs:

$$u_{max} \quad \begin{cases} = 0.011\alpha^{0.4}L^{0.9}B^{0.1}P^{-0.1} + 0.08 & \text{for } H \le 13\text{ft} \\ = 0.022\alpha + 0.001L - 0.011B - 0.163P + 0.68 & \text{for } 13 \le H \le 18\text{ft} \\ = 1.5\alpha^{0.02}L^{-0.1}B^{0.1}P^{-0.1} + 0.096 & \text{for } H \ge 18\text{ft} \end{cases} \qquad (14)$$

where: u_{max} = maximum pile-head displacement (in), α = thermal expansion coefficient (in/in/ºF) × 1E+6, L = total bridge length (ft), H = backfill height (ft) in Fig. 9, B = backfill stiffness in Table 3 (*Low* = 1, *Intermediate* = 2, *High* = 3), P = soil pile stiffness in Table 4 (*Low* = 1, *Intermediate* = 2, *High* = 3).

Fig. 12 presents pile head displacement for different backfill heights based on bridge length. The graph is based on α = 6.0 in/in/°F for concrete girder bridges and α = 6.5 in/in/°F for steel girder bridges and with intermediate backfill stiffness. For comparison purposes, free expansion is also plotted based on α = 6.0 in/in/°F and a 70°F temperature change for concrete girder bridges and 120°F temperature change for steel girder bridges (AASHTO LRFD, 2010).

Minimum Number of Laterally Supporting Piles

Fig. 13 demonstrates the effect of the number of piles, N_p, and is used to determine the minimum number supporting piles. IAB abutment height versus bridge length is plotted. All IABs plotted on this graph must be below and to the right of each curve to prevent pile yielding due to thermal loading. The developed plots are based on the assumption that 50 percent of pile section yielding capacity (F_y = 50 ksi) is consumed by thermal loading and α = 6.0 in/in/°F. When backfill height is high and soil pile stiffness is low, the pile bending moment decreases. However, as soil pile stiffness increases, the pile bending moment rapidly increases.

Superstructure Moments

Positive and negative moments due to thermal loading and time-dependent effects occur throughout the superstructure. During bridge contraction, maximum positive moment occurs at mid-span in the end span and the maximum negative moment occurs adjacent to the abutment. During bridge expansion, a negative moment occurs at mid-span in the end span and a positive moment occurs adjacent to the abutment. Positive and negative girder moments at the abutment are always larger at mid-span. The maximum bridge total positive and negative moments are estimated at the girder end adjacent to the abutment in Equations (15) through (23) as:

For prestressed concrete girder IABs:

$$\begin{aligned} M_{pos} &= 120\alpha - 190H + 690P - 14 \geq 0 && \text{for } L \leq 130\text{ft} \\ &= 210\alpha + 53H + 170P - 3400 \geq 0 && \text{for } 130 \leq L \leq 300\text{ft} \\ &= 59\alpha + 740P - 2600 \geq 0 && \text{for } L \geq 300\text{ft} \end{aligned} \quad (15)$$

$$\begin{aligned} M_{neg} &= -74\alpha^{0.35}L^{0.6}P^{0.2} && \text{for } H \leq 13\text{ft} \\ &= -280\alpha^{0.4}L^{0.35} && \text{for } 13 \leq H \leq 18\text{ft} \\ &= -4000\alpha^{0.1}P^{-0.4} && \text{for } H \geq 18\text{ft} \end{aligned} \quad (16)$$

For steel girder IABs:

$$M_{pos} = -12\alpha + 3L - 208H - 10B + 863P + 1570 \geq 0 \quad (17)$$

$$M_{neg} = -158\alpha^{0.2}L^{0.7}H^{0.3}B^{0.1}P^{-0.2} - 1990 \quad (18)$$

and at the girder mid-span in the end span (in a multi-span IAB) as:

For prestressed concrete girder IABs:

$$\begin{aligned} M_{pos} &= 134\alpha + 11L + 1040P - 3300 \geq 0 && \text{for } H \leq 13\text{ft} \\ &= 118\alpha + 13L + 1100P - 4000 \geq 0 && \text{for } 13 \leq H \leq 18\text{ft} \\ &= 213\alpha + 14L + 1500P - 6700 \geq 0 && \text{for } H \geq 18\text{ft} \end{aligned} \quad (19)$$

$$\begin{aligned} M_{neg} &= -17\alpha^{0.7}L^{0.80}B^{0.1}P^{0.3} && \text{for } H \leq 13\text{ft} \\ &= -26\alpha^{1.0}L^{0.65}B^{0.1}P^{-0.08} && \text{for } 13 \leq H \leq 18\text{ft} \\ &= -700\alpha^{0.55}L^{0.25}B^{0.04}P^{-0.7} && \text{for } H \geq 18\text{ft} \end{aligned} \quad (20)$$

For steel girder IABs:

$$M_{pos} = -166\alpha + 0.5L - 5.9H - 5.6B + 269P + 1803 \quad (21)$$

$$M_{neg} = 179\alpha - 4.5L + 17.5H - 40.9B + 156P - 2480 \quad (22)$$

$$M_g = \frac{M_{pos} \text{ or } M_{neg}}{N_g} \quad (23)$$

where: M_{pos} = bridge total positive moment (kip-ft), M_{neg} = bridge total negative moment (kip-ft), M_g = girder moment (kip-ft), N_g = number of girders, α = thermal expansion coefficient (in/in/ºF) × 1E+6, L = total bridge length (ft), H = backfill height (ft), B = backfill stiffness (*Low* = 1, *Intermediate* = 2, *High* = 3), P = soil pile stiffness in (*Low* = 1, *Intermediate* = 2, *High* = 3).

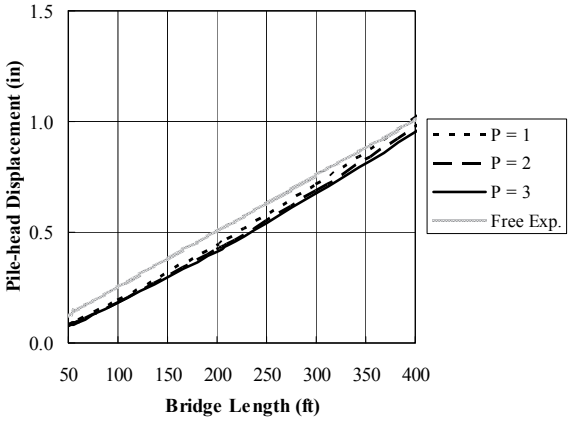

(a) Prestressed Concrete Girder IAB:
Backfill Height (*H*) = 10 ft (3.05 m)

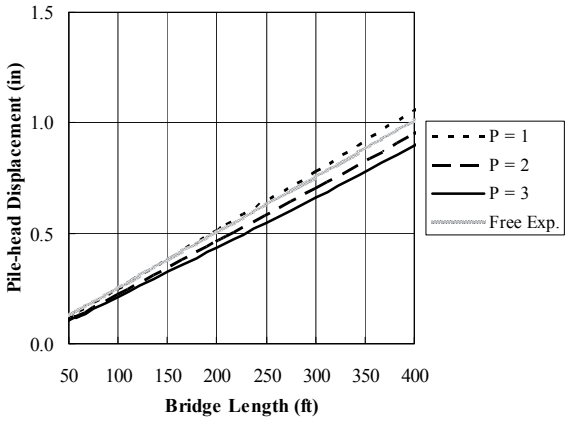

(b) Prestressed Concrete Girder IAB:
Backfill Height (*H*) = 15 ft (4.57 m)

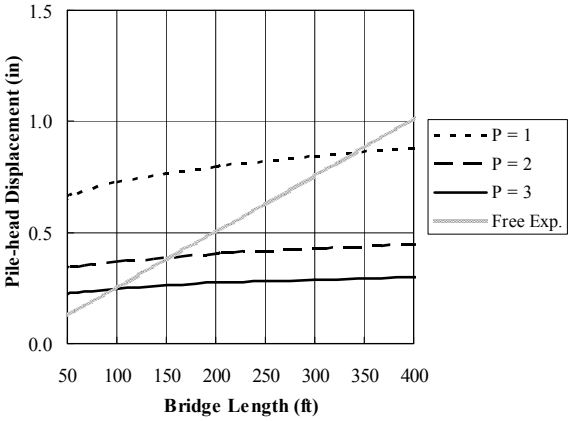

(c) Prestressed Concrete Girder IAB:
Backfill Height (*H*) = 20 ft (6.10 m)

Fig. 12—Maximum Pile Head Displacement (1 in = 25.4 mm).

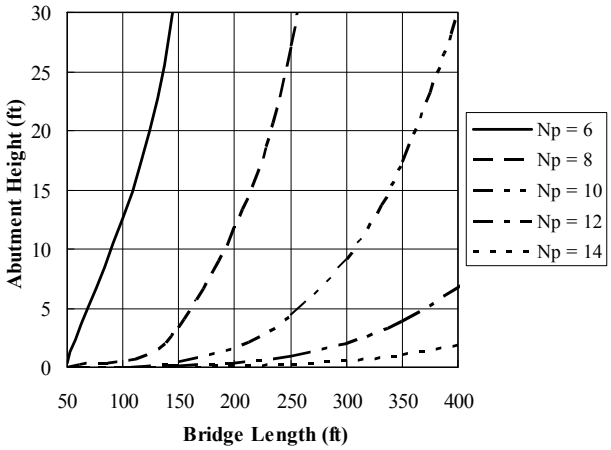

(a) Prestressed Concrete Girder IAB:
Soil Pile Stiffness (*P*) = *Low*

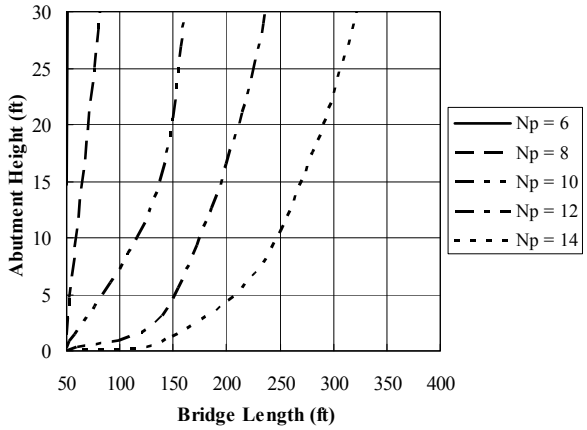

(b) Prestressed Concrete Girder IAB:
Soil Pile Stiffness (*P*) = *Intermediate*

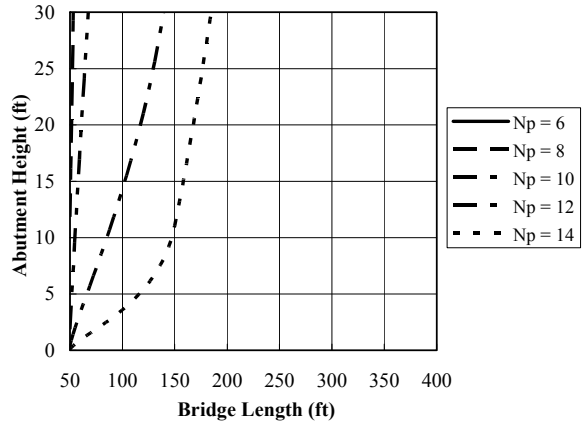

(c) Prestressed Concrete Girder IAB:
Soil Pile Stiffness (*P*) = *High*

Fig. 13—Minimum Required Number of Piles (1 ft = 0.305 m).

Bridge Total Bending Moment

Figures 14 and 15 present bridge total positive and negative bending moments at mid-span of the exterior span. Figures 16 and 17 present bridge total positive and negative bending moments at the abutment. Bridge total bending moments are determined based on bridge length (L) and backfill height (H). Bridge total positive bending moments at mid-span are a function of three bridge lengths: 60 ft, 200 ft, and 400 ft. Bridge total negative bending moments at girder mid-span are a function of three backfill heights: 10 ft, 15 ft, and 20 ft. Bridge total positive and negative bending moments at the abutment are also a function of backfill height.

Maximum Pile Head Moments

H-pile head moments (at the top of the pile) are critical in determining required pile strength. Fig. 13 illustrates calculated pile head response with respect to the lateral loading at the pile head. The maximum pile head moments resisted by the piles are estimated as follows:

For prestressed concrete girder IABs:

$$\Sigma M_{piles} = 21\alpha^{0.5}L^{0.5}H^{0.1}P^{0.6} \leq M_{y\,pile}\,N_p \tag{24}$$

For steel girder IABs:

$$\begin{aligned} \Sigma M_{piles} &= 12\alpha^{0.4}L^{0.6}P^{0.5} + 203 && \text{for } H \leq 13\text{ft} \\ &= 30\alpha^{0.4}L^{0.4}P^{0.5} + 287 && \text{for } 13 \leq H \leq 18\text{ft} \\ &= 223\alpha^{0.3}L^{0.2}P^{0.2} + 324 && \text{for } H \geq 18\text{ft} \end{aligned} \tag{25}$$

$$M_{pile} = \frac{\Sigma M_{piles}}{N_p} \tag{26}$$

where: ΣM_{piles} = total moment resisted by the piles (kip-ft), $M_{y\,pile}$ = single pile yielding moment (kip-ft), N_p = number of piles, M_{pile} = maximum single pile moment (kip-ft), α = thermal expansion coefficient (in/in/ºF) × 1E+6, L = total bridge length (ft), H = backfill height (ft), B = backfill stiffness (*Low* = 1, *Intermediate* = 2, *High* = 3), P = soil pile stiffness (*Low* = 1, *Intermediate* = 2, *High* = 3).

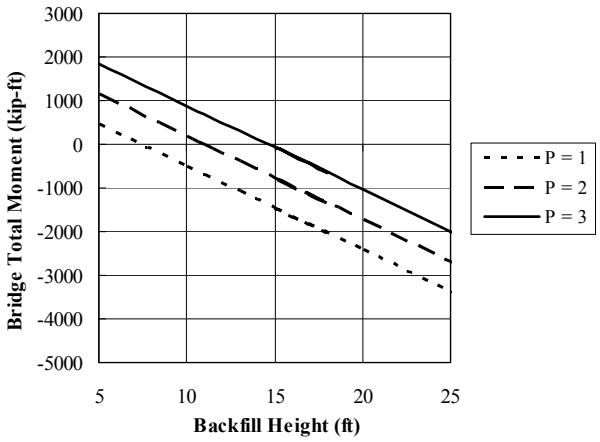

(a) Prestressed Concrete Girder IAB:
Bridge Length (L) = 60ft (18.3 m)

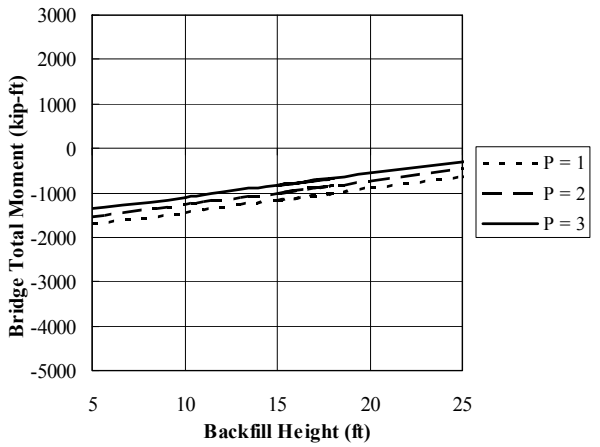

(b) Prestressed Concrete Girder IAB:
Bridge Length (L) = 200ft (61.0 m)

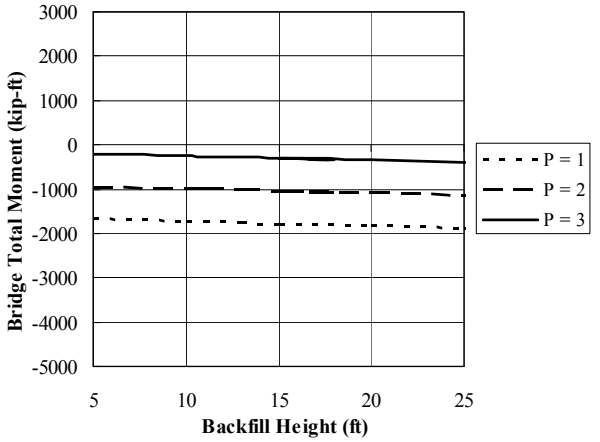

(c) Prestressed Concrete Girder IAB:
Bridge Length (L) = 400ft (121.9 m)

Fig. 14— Bridge Total Positive Bending Moment at Mid-Span of the Exterior Span.

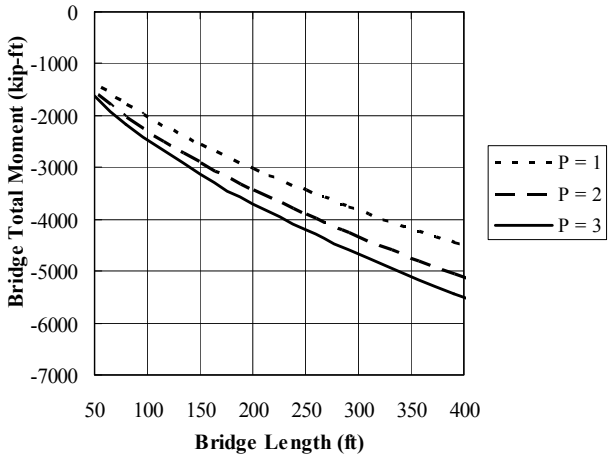

(a) Prestressed Concrete Girder IAB:
Backfill Height (H) = 10 ft (3.05 m)

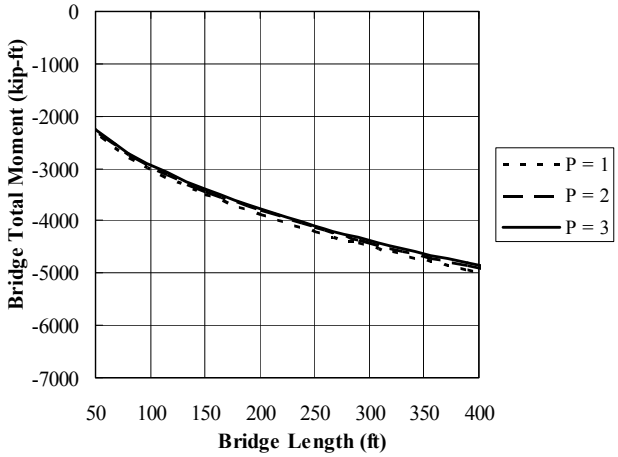

(b) Prestressed Concrete Girder IAB:
Backfill Height (H) = 15 ft (4.57 m)

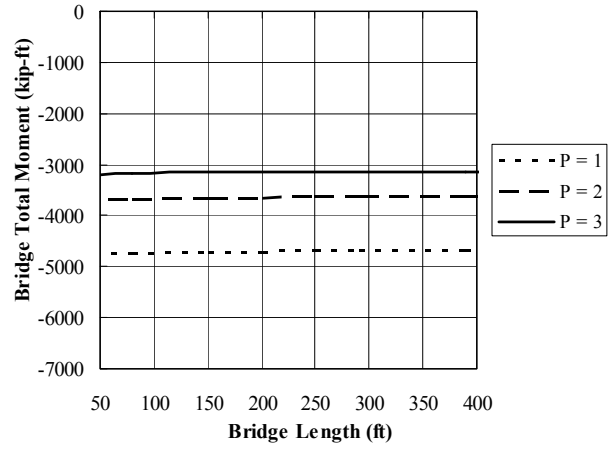

(c) Prestressed Concrete Girder IAB:
Backfill Height (H) = 20 ft (6.10 m)

Fig. 15— Bridge Total Negative Bending Moment at Mid-Span of the Exterior Span.

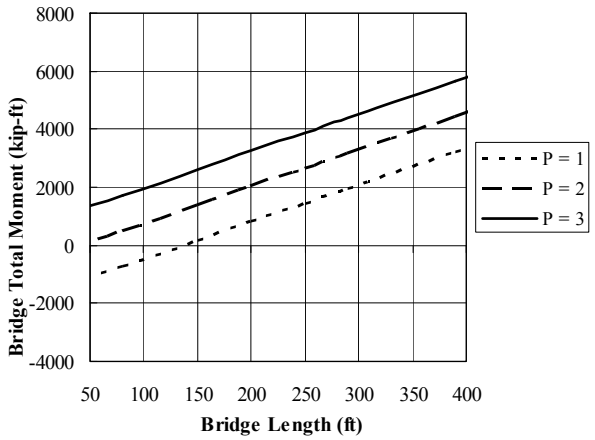

(a) Prestressed Concrete Girder IAB: Backfill Height (H) = 10 ft (3.05 m)

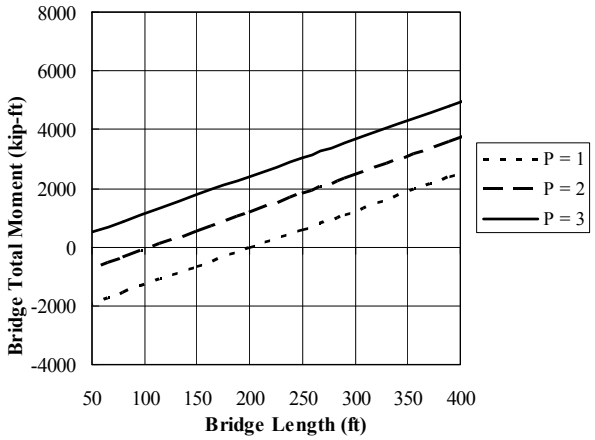

(b) Prestressed Concrete Girder IAB: Backfill Height (H) = 15 ft (4.57 m)

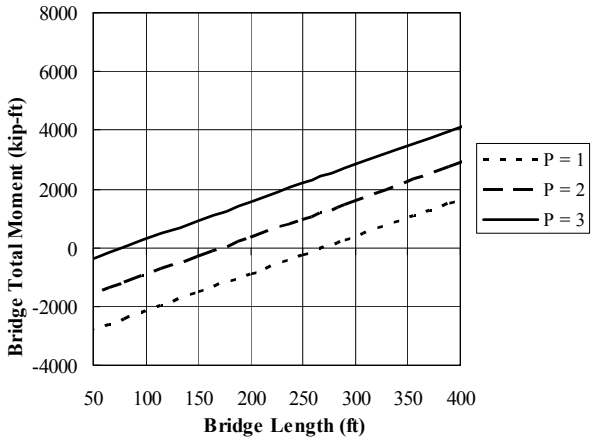

(c) Prestressed Concrete Girder IAB: Bridge Length (L) = 400ft (6.10 m)

Fig. 16—Bridge Total Positive Bending Moment at Abutment.

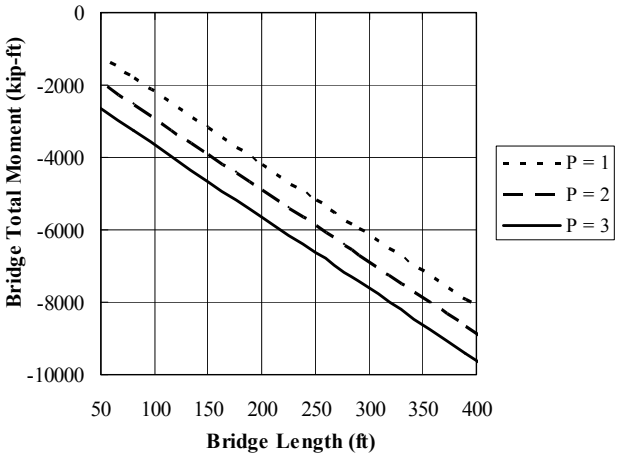

(a) Prestressed Concrete Girder IAB: Backfill Height (H) = 10ft (3.05 m)

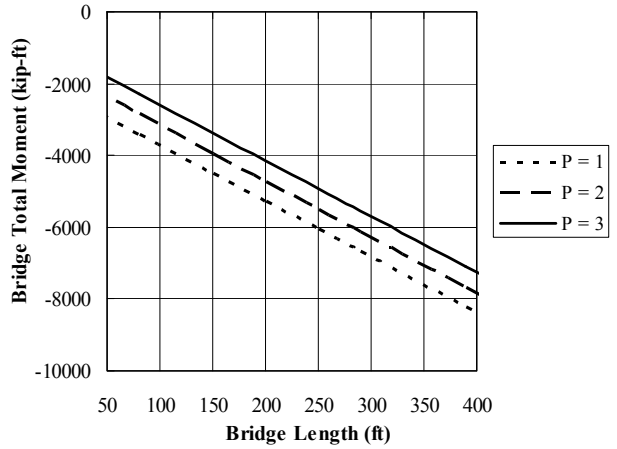

(b) Prestressed Concrete Girder IAB: Backfill Height (H) = 15ft (4.57 m)

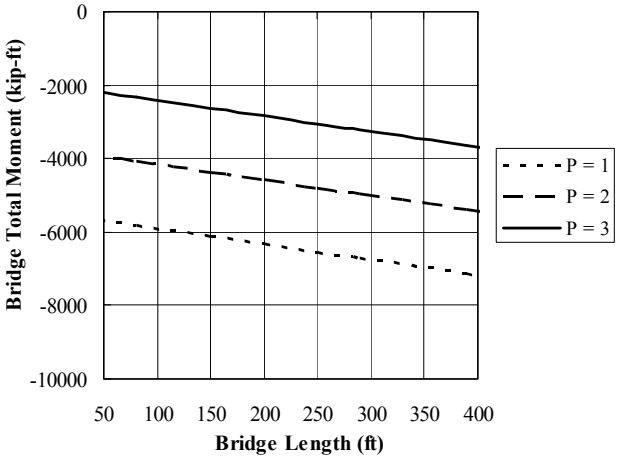

(c) Prestressed Concrete Girder IAB: Backfill Height (H) = 20 ft (6.10 m)

Fig. 17—Bridge Total Negative Bending Moment at Abutment.

SUMMARY AND CONCLUSIONS

Based on the presented study, the following conclusions are offered:

1. Steel girders and a tall abutment tend to reduce the girder tensile axial force. Prestressed concrete girders, hinged abutment-to-backwall joints, and low backfill height tend to reduce girder compressive axial force.

2. Accounting for the axial tensile force in a prestressed concrete girder is generally more critical than the compressive axial force and can be considered using the proposed method.

3. A hinged construction joint, low abutment height and short bridge length reduce the girder positive moment. A negative girder moment counteracts gravity loads and, therefore, is not of concern.

4. A rigid abutment-to-backwall joint and high abutment height increase the negative girder moment.

5. A prestressed concrete girder, PennDOT type abutment-to-backwall joint, and low abutment height are effective in reducing pile moments.

6. A hinged abutment-to-backwall joint reduces pile moment for bridge contraction, and a rigid connection tends to reduce pile moments under bridge expansion.

7. A prestressed concrete girder, PennDOT standard abutment-to-backwall joint and short bridge length reduce the pile lateral force.

8. A hinged abutment-to-backwall joint connection tends to reduce the pile lateral force under bridge contraction. Under bridge expansion, the pile lateral force increases for a hinged construction joint and decreases for a rigid construction joint.

9. A hinged construction joint and high abutment height tends to reduce pile head displacement in IABs.

An approximate analysis method has been proposed that is based on field monitoring results and numerical modeling methodology of the above-discussed parametric study. The approximate analysis method allows the generalization of predicted integral abutment bridge behavior within certain limitations. The studied parameters considered in the parametric study (thermal expansion coefficient, bridge length, backfill height, backfill stiffness, and pile soil stiffness) are inputs to the approximate analysis that predicts key responses through the use of best-fit curves. Extensive numerical simulations resulted in a large dataset for analysis and curve fitting: three ranges for each parameter resulted in 243 parametric study cases for both prestressed concrete girder bridges and steel girder bridges. A total of 486 separate study cases were analyzed for a 75-year time-history analysis to account for long-term effects. The established approximate analysis methods include: (1) maximum (tensile) girder axial force; (2) minimum (compressive) girder axial force; (3) maximum (positive) girder moment at the girder end adjacent to the abutment; (4) minimum (negative) girder moment at the girder end adjacent to the abutment; (5) maximum girder moment at the girder mid-span in the end span; (6) minimum girder moment at the girder mid-span in the end span; (7) pile lateral force; (8) pile moment; and (9) pile head displacement. Each approximate analysis prediction is strongly correlated to a numerical analysis result, exhibiting approximately more than 80% correlation.

REFERENCES

1. Laman, J. A., and Kim, W. "Monitoring of Integral Abutment Bridges and Design Criteria Development," *Final Report No. FHWA-PA-2009-005-PSU002*, Pennsylvania Transportation Research Council, 2009, 650pp.
2. Laman, J. A., Pugasap, K., and Kim, W. "Field Monitoring of Integral Abutment Bridges," *Final Report No. FHWA-PA-2006-006-510401-01*, Pennsylvania Transportation Research Council, 2006, 293 pp.
3. Kim, W., and Laman, J. A. "Long-term Field Monitoring of Four Integral Abutment Bridges," the Transportation Research Board of the National Academies, 89th Annual Meeting Compendium, DVD, paper #10-0810, 2010, January 10-14, Washington, D.C.
4. PennDOT Design Manual Part 4 (2000) "Structures: Procedures-Design-Plans Presentation," Commonwealth of Pennsylvania, Department of Transportation, V. 1.
5. ANSYS Release 11.0. ANSYS University Advanced, ANSYS Inc. 2005.
6. Kim, W., and Laman, J. A. (2010) "Numerical Analysis Method for Long-term Behavior of Integral Abutment Bridges," *Engineering Structures*, Vol. 32, Issue 8, August, pp. 2247-2257.
7. Kim, W., and Laman, J. A. (2010) "Integral Abutment Bridge Response under Thermal Loading," *Engineering Structures,* Vol. 32, Issue 6, June, pp. 1495-1508.
8. Pugasap, K., Kim, W., and Laman, J. A. (2009) "Long-Term Response Prediction of Integral Abutment Bridges," *Journal of Bridge Engineering*, ASCE, Vol. 14, No. 2, Mar./Apr. pp.129-139.
9. Taciroglu, E., Rha, C., Stewart, J. P., and Wallace, J. W. (2003) "Robust Numerical Models for Cyclic Response of Columns Embedded in Soil," The 16th ASCE Engineering Mechanics Conference, University of Washington, Seattle, July 16-18.
10. Boulanger, R. W., Curras, C. J., Kutter, B. L., Wilson, D. W., and Abghari, A. (1999) "Seismic Soil-Pile-Structure Interaction Experiments and Analyses," *Journal of Geotechnical and Geoenvironmental Engineering*, ASCE, V. 125, No. 9, pp. 750-759.
11. Paul, M. D., Laman, J. A., and Linzell, D. G. (2005) "Thermally Induced Superstructure Stresses in Prestressed Girder Integral Abutment Bridges," *Transportation Research Record: Journal of the Transportation Research Board*, Transportation Research Board of the National Academies, Washington D.C., pp. 287-297.
12. American Association of State Highway and Transportation Officials (AASHTO LRFD). (2010). *AASHTO LRFD Bridge Design Specifications*, Washington, D.C.
13. Comite Euro-Internationale du Beton (CEB) (1990). *CEB-FIP Model Code for Concrete Structures*, *Buletin D'Information* No. 213/214, Lausanne, Switzerland.
14. American Concrete Institute Committee 209 (ACI 209). (2004). "Prediction of Creep, Shrinkage, and Temperature Effects in Concrete Structures," *ACI Manual of Concrete Practice Part I*, American Concrete Institute, Farmington Hills, MI.
15. Jirásek, M. and Bažant, Z. P. (2002). "Inelastic Analysis of Structures," John Wiley & Sons, New York.
16. Ghali, A., Favre, R., and Elbadry, M. (2002). Concrete Structures: Stresses and Deformation, 3th Ed., Spon Press, London.